Multimodal Biomedical Imaging with Asymmetric Single-Walled Carbon Nanotube/Iron Oxide Nanoparticle Complexes

Jong Hyun Choi,[†] **Freddy T. Nguyen,**[‡,§,||,#] **Paul W. Barone,**[†] **Daniel A. Heller,**[‡,#]
Anthonie E. Moll,[†] **Dhaval Patel,**[†] **Stephen A. Boppart,**[||,⊥,#] **and**
Michael S. Strano*,[†,#]

Department of Chemical and Biomolecular Engineering, Department of Chemistry, Medical Scholars Program, College of Medicine, Departments of Electrical and Computer Engineering and Bioengineering, Beckman Institute for Advanced Science and Technology, University of Illinois at Urbana/Champaign, Urbana, Illinois 61801

ABSTRACT

Magnetic iron oxide nanoparticles and near-infrared (NIR) fluorescent single-walled carbon nanotubes (SWNT) form heterostructured complexes that can be utilized as multimodal bioimaging agents. Fe catalyst-grown SWNT were individually dispersed in aqueous solution via encapsulation by oligonucleotides with the sequence d(GT)$_{15}$, and enriched using a 0.5 T magnetic array. The resulting nanotube complexes show distinct NIR fluorescence, Raman scattering, and visible/NIR absorbance features, corresponding to the various nanotube species. AFM and cryo-TEM images show DNA-encapsulated complexes composed of a ∼3 nm particle attached to a carbon nanotube on one end. X-ray diffraction (XRD) and superconducting quantum interference device (SQUID) measurements reveal that the nanoparticles are primarily Fe_2O_3 and superparamagnetic. The Fe_2O_3 particle-enriched nanotube solution has a magnetic particle content of ∼35 wt %, a magnetization saturation of ∼56 emu/g, and a magnetic relaxation time scale ratio (T_1/T_2) of approximately 12. These complexes have a longer spin−spin relaxation time ($T_2 \sim$ 164 ms) than typical ferromagnetic particles due to the smaller size of their magnetic component while still retaining SWNT optical signatures. Macrophage cells that engulf the DNA-wrapped complexes were imaged using magnetic resonance imaging (MRI) and NIR mapping, demonstrating that these multifunctional nanostructures could potentially be useful in multimodal biomedical imaging.

Introduction. Single-walled carbon nanotubes (SWNT) exhibit unique electrical and optical properties, including large Raman scattering cross-sections, near-infrared (NIR) fluorescence, and UV/visible/NIR absorption.[1−9] Each optical transition corresponds to a specific nanotube species that is identified by a chirality vector, (*n,m*) which defines the chirality of SWNT, as they are conceptually rolled-up graphene sheets.[2] The optical properties of SWNT make them appealing as biological sensors and imaging contrast agents because their NIR photoluminescence (PL) lies within the "biological window" (700−1300 nm) where absorption, scattering, and autofluorescence by tissues, blood, and water are minimized.[10,11] Note that the PL of SWNT is observed only when they are individually dispersed.[12,13] Previous studies have shown that carbon nanotubes can be individually suspended using surfactants,[12,13] polymers,[14] proteins,[3,15] phospholipids,[16] and DNA oligonucleotides[10,17−19] in aqueous solution, making them biocompatible as well. We have shown that SWNT wrapped by DNA oligonucleotides are engulfed by living cells through endocytosis and remain fluorescent without significant photobleaching,[10] suggesting that they can be used as viable biomedical imaging agents.[19]

Iron oxide nanoparticles have been studied extensively as magnetic resonance imaging (MRI) contrast agents and mediators for cancer magnetic hyperthermia.[20−23] In MRI, iron oxide particles induce dephasing of proton spin by energy exchange between the atomic nuclei, resulting in the decrease of spin−spin relaxation time, T_2, and thus creating the image contrast. These magnetic nanoparticles have much higher relaxivities than Gd(III)-chelating molecules, which are often used for spin−lattice relaxation time T_1-weighted imaging.[20,22,24] Dextran-coated iron oxide particles are less toxic than pristine iron oxide particles due to a biocompatible

* Corresponding author. E-mail: strano@uiuc.edu.
† Department of Chemical and Biomolecular Engineering.
‡ Department of Chemistry.
§ Medical Scholars Program.
|| College of Medicine.
⊥ Departments of Electrical and Computer Engineering and Bioengineering.
Beckman Institute for Advanced Science and Technology.

surface coating and thus have an order of magnitude higher lethal dose level (LD$_{50}$).[23] We have demonstrated that iron oxide nanoparticles can be used as potential contrast agents for magnetomotive optical coherence tomography (MM-OCT).[25,26] A modulated external magnetic field induces the motion of the magnetic particles, thereby modifying the overall scattering properties. By locking onto the modulation frequency and by comparing the scattering signals when the field is on and off, one can increase the observed OCT contrast, which can be used for in vivo imaging.[26]

The development of multifunctional nanoparticles in biomedical imaging has become more critical as the need arises for nanoparticles to detect, diagnose, monitor, and treat diseases. These nanoparticles would complement current imaging technologies by providing higher sensitivity and specificity, with the long-term goal of providing patients with earlier and more localized treatment options. Recently, magnetic and optical nanomaterials have been studied actively for this purpose.[27−33] In many of these studies, however, organic fluorophores were used as fluorescent labels that easily photobleach in live cells.[10,29] In the present study, we demonstrate for the first time the multifuntionality of single-walled carbon nanotube/iron oxide nanoparticle complexes as dual magnetic and fluorescent imaging agents. By encapsulation with DNA, the SWNT/iron oxide nanoparticle complexes are individually dispersed in aqueous solution and are more easily introduced into a biological environment. The iron oxide nanoparticle is located specifically at only one end of the SWNT in an asymmetric arrangement. We characterize the optical properties using Raman, absorption, and photoluminescence spectroscopy, while the magnetic properties are investigated with superconducting quantum interference device (SQUID). We show 2-D in vitro images of murine macrophage cells with these nanostructures using magnetic resonance and near-infrared mapping.

Experimental. We obtained SWNT from the Rice University Research Reactor (Run 107), which were produced by chemical vapor deposition (CVD) with continuously flowing CO as the carbon feedstock and a small amount of Fe(CO)$_5$ as the iron-containing catalyst precursor at high pressure (30−50 atm), called the HiPco process.[34,35] The process results in iron oxide nanoparticles attached to one end of the nanotube. The SWNT dispersion process using DNA was slightly modified from the method previously described.[17,18] Briefly, 1 mg of the as-prepared SWNT was mixed with 1 mg of a 30-mer custom-synthesized DNA sequence of alternating guanine and thymine amino acids, d(GT)$_{15}$, (Integrated DNA Technologies) in 1 mL of 0.1 M NaCl solution. The mixture solution was ultrasonicated in a water bath (Branson 1510) for 60 min and centrifuged at 16 000g (Spectrafuge 24D, Labnet International Inc.) for an additional 90 min. The supernatant was transferred to a Petri dish placed over an array of ∼0.5 T magnets. After 2 days, the SWNT/iron oxide nanoparticle complexes aggregated along the boundary between adjacent magnets where the magnetic field gradient was at its highest, as shown in Figure 1a. These aggregates were pipetted out and redispersed by
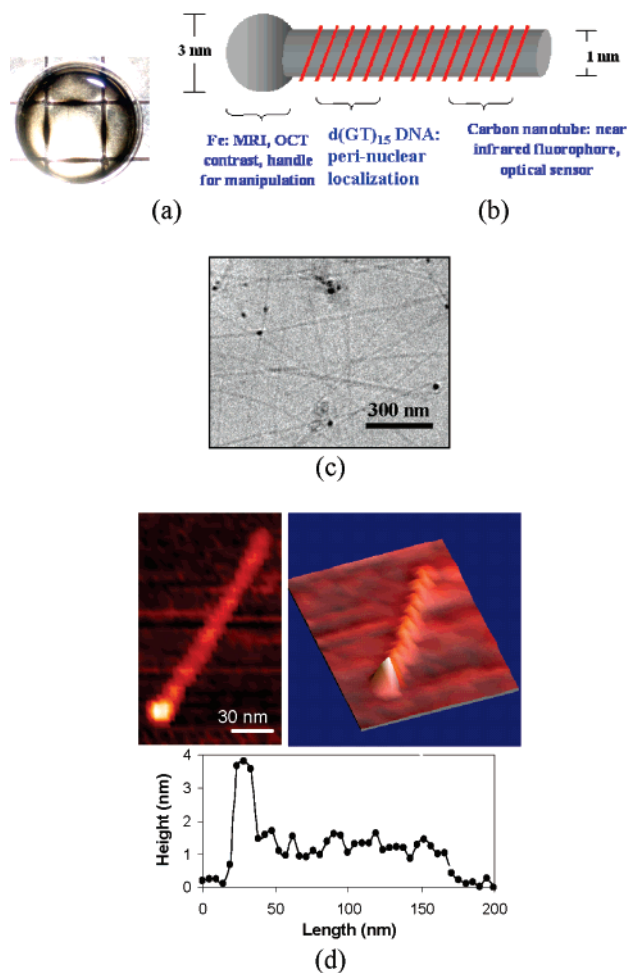

Figure 1. (a) Separation process of single-walled carbon nanotube/iron oxide nanoparticle solution over a ∼0.5 T magnetic array. (b) Schematic of the DNA-wrapped nanotube/iron oxide nanoparticle complex. DNA wrapping renders SWNT water-soluble and biocompatible, and aids cellular uptake by endocytosis. (c) A cryogenic-TEM image showing the heterostructured complexes of the SWNT/iron oxide nanoparticles. (d) 2-D and 3-D AFM images of a complex encapsulated by DNA. The 3-D view shows DNA wrapping of a carbon nanotube. The height profile along the nanotube reveals that the catalyst particle is 3−4 nm in diameter, the nanotube diameter is ∼1 nm, and DNA pitch ranges from 12 to 20 nm.

ultrasonication for 1 min. This magnetic separation process was repeated five times for further purification. The initial, iron oxide particle-enriched (Fe-enriched) and iron oxide particle-depleted (Fe-depleted) DNA-SWNT samples were prepared with nanotube concentrations of 137, 154, and 159 mg/L, respectively.

A Shimadzu UV-3101PC absorption spectrometer measured the absorbance of the samples from 190 to 1400 nm. With a 632.8 nm HeNe laser as the excitation source, the NIR fluorescence spectra from SWNT were monitored from 900 to 1400 nm using a liquid N$_2$-cooled InGaAs array detector (OMA V, Princeton Instruments). The Raman signatures and NIR mapping of SWNT were recorded using a Raman spectrometer with a 785 nm excitation from a laser diode (Kaiser Optical Systems Inc.). A cryogenic transmission electron microscope (TEM) and an atomic force

microscope (AFM, NanoScope IIIa) were used to visualize the SWNT/iron oxide nanoparticle complexes. The crystal structures of the samples were analyzed with a Rigaku D/Max-B X-ray diffractometer (XRD, Cu Kα radiation: $\lambda_{average} = 1.5418$ Å). For XRD sample preparation, the nanotube solution samples containing the same amount of nanotubes (∼1 mL) were flocculated using acetone, and the precipitates were deposited onto glass slides. The XRD patterns of the dried samples were recorded for the measurement angle, 2θ from 15° to 70°. A superconducting quantum interference device (1 T magnetic property measurement systems, Quantum Design) was used to characterize the magnetization properties of the SWNT/iron oxide nanoparticle samples. Approximately 0.65 μg of each of the three prepared nanotube samples was deposited and dried onto individual sheets of Parafilm and encapsulated into a gel cap for SQUID analysis. The measurements were made at 298 K using a magnetic field from −1 to +1 T.

Murine macrophage cells (RAW 264.7) were cultured for MR imaging and NIR mapping. The cultured cells were incubated for approximately 7 h with the nanostructure samples in the cell media, HEPES (4-(2-hydroxyethyl)-1-piperazineethanesulfonic acid)-buffered Dulbecco's minimal essential media (DMEM, Cellgro 15-018 CV; Mediatech, Herndon, VA) supplemented with 10% fetal bovine serum (FBS, Sigma) and 1% antibiotics.[10] After the incubation, these cells were washed with 8 mL of phosphate-buffered saline (PBS) and resuspended in the cell media to ensure that any sample materials present would be in the cells and not floating free in the media. The cells were then transferred to 2 mm diameter tubes for MRI and onto glass slides for NIR mapping. MR imaging of the incubated cells was performed at the Biomedical Imaging Center of the Beckman Institute (14.1 T Varian, 600 MHz). Magnetic relaxation time scales were also measured from the samples with different iron contents in Intralipid (Fresenius Kabi, Uppsala, Sweden), a scattering optical solution commonly used as an optical equivalent for human tissue.

Results and Discussion. High-quality SWNTs are often grown by disproportionation of carbon-containing molecules (CO or C_2H_4) using premade metal catalyst nanoparticles such as Mo.[36,37] The HiPco SWNT used in this study are produced by thermal decomposition in the gas phase, where iron clusters are generated from $Fe(CO)_5$, and carbon atoms from CO catalytically nucleate to form SWNT and grow in length on the cluster surface.[34,35] The nanotube growth is terminated when the iron clusters become too large (relative to the SWNT diameter, e.g., ∼1 nm) and overcoated with amorphous carbon or evaporate at a high temperature. The final nanotube product includes 2−5 nm iron particles, with a typical carbon to iron mol % ratio of 97:3.[35] The individually dispersed nanotube has one Fe particle on its end, as the schematic shows in Figure 1b. In practice, only a fraction of SWNT are attached to the magnetic particles because either the growth of some nanotubes is terminated by evaporation of the catalysts as described above or the iron nanoparticles may detach during the ultrasonication processing. The cryogenic-TEM image (Figure 1c) shows the heterostructured complexes composed of catalyst nanoparticles attached to single-walled carbon nanotubes. The AFM images in Figure 1d confirm complex conjugation with DNA. The three-dimensional (3-D) view shows DNA wrapping of the carbon nanotube, where it was modeled that the DNA bases are conjugated with a carbon nanotube surface through a stacking interaction and the DNA sugar−phosphate backbone on the exterior renders the hybrid complex water-soluble.[17] The AFM height profile along the nanotube reveals that the catalyst particle is 3−4 nm in diameter, the nanotube diameter is ∼1 nm, and the DNA pitch ranges from 12 to 20 nm.[18]

Figure 2 presents UV/vis/NIR absorption, photoluminescence (PL), and Raman spectra of the initial, Fe-enriched, and Fe-depleted DNA-SWNT samples in water. The absorption spectra in Figure 2a are offset for comparison, and the PL spectra are corrected for the sample concentrations. The three absorption spectra are not significantly different and clearly show the electronic transitions of metallic and semiconducting nanotube species throughout the visible and near-infrared. In the PL spectra (Figure 2b), seven distinct features are observed and assigned to seven semiconducting nanotube species as denoted in the figure. These peaks are red-shifted by 15−25 nm, compared to sodium dodecyl sulfate-suspended SWNT.[2] The discrete optical signatures in both the absorbance and PL spectra indicate that these DNA-wrapped SWNTs are individually suspended. Note that the Fe-enriched sample has approximately half the PL intensity of the other two samples below 1200 nm, whereas the Fe-depleted spectrum becomes similar to the Fe-enriched one above 1200 nm. The nanotube species emitting fluorescence from 900 to 1200 nm have smaller diameters than (8,6) and (10,3) nanotubes. This implies that either the Fe-enriched sample contains fewer nanotubes with smaller diameters than the other two samples or more quenching occurs in those tubes. Our previous study demonstrated that probe-tip sonication cuts a greater proportion of SWNT with larger diameter than that of smaller ones.[38] In this work, we used a bath sonicator that does not cut a significant fraction of nanotubes, so the lower content of small-diameter SWNTs in the Fe-enriched sample is not due to the severe nanotube cutting during the ultrasonication. Possible scenarios include more detaching of the catalyst particles from small-diameter nanotubes and increased PL quenching from the magnetic cluster in smaller-diameter SWNTs. The relation between the PL and morphology of the complexes needs more rigorous investigation. Nonetheless, the Fe-enriched SWNTs have comparable luminescence throughout the near-infrared to the initial and Fe-depleted samples.

Raman signatures in Figure 2c include the radial-breathing modes (RBM) from 200 to 300 cm^{-1}, and G and G' peaks near 1590 and 2590 cm^{-1}, respectively. These Raman spectra are normalized by the G peak (tangential mode of graphene structures) at 1592 cm^{-1}. Five nanotube fluorescence features are also observed as assigned in the figure. As seen in the PL spectra, the (8,3), (6,5), and (7,5) nanotube peaks of the initial and Fe-depleted samples are similar and higher than those of the Fe-enriched sample. In all three samples, we do
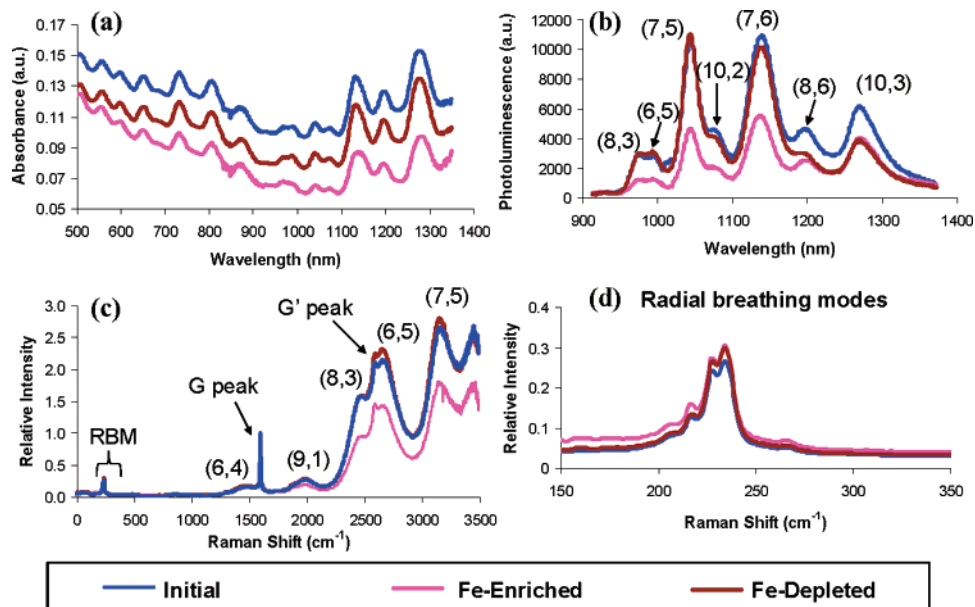
Figure 2. (a) Absorption, (b) photoluminescence, (c) Raman spectra, and (d) radial breathing modes of the initial, Fe-enriched, and Fe-depleted nanotube samples. The absorbance spectra of the three samples are offset for clarity. The PL and Raman spectra are normalized with respect to the nanotube concentrations and G peak, respectively. The overall optical properties of these samples are not significantly different.

not observe a distinct peak near 267 cm^{-1} in Figure 2d, indicative of the absence of nanotube aggregates in the solution: nanotube bundles cause the lowering and broadening in the interband transition energies, resulting in the intensities of the Raman shift to change depending on the nanotube species and the excitation energy.[39]

The crystal structures of the initial, Fe-enriched, and Fe-depleted samples are examined by X-ray diffraction in Figure 3a. The most prominent XRD feature in the Fe-enriched sample is Fe_2O_3 (JCPDS 89-0599, 39-1346). The other peak is assigned to either the iron in the [111] plane (JCPDS 88-2324), iron carbide (Fe_3C) in the [103] plane (JCPDS 76-1877), or both. These XRD features were also observed with iron oxide-filled multiwalled carbon nanotubes grown by pyrolysis of ferrocene.[40] In the initial sample, the Fe_2O_3 and Fe/Fe_3C peaks are reduced significantly. The iron oxide feature further decreases and the Fe/Fe_3C signature is no longer observed in the Fe-depleted sample, indicating that, although the Fe-depleted DNA-SWNT sample is not completely free of the magnetic nanoparticles, the content is significantly lower than the Fe-enriched sample. The iron content of the initial sample is between the Fe-enriched and Fe-depleted samples because we separate the SWNT/iron oxide nanoparticle complexes from it. On the basis of this XRD pattern and our previous X-ray photoelectron spectroscopic (XPS) results of the initial SWNT,[41] we estimate that the iron oxide particle contents are 35, 16, and 11% by weight in the Fe-enriched, initial, and Fe-depleted samples, respectively.

SQUID measurements reveal the magnetic characteristics of the SWNT samples (Figure 3b). The Fe-enriched SWNT require the lowest magnetic field (∼0.4 T) to reach their magnetization saturation (M_s), which is several times stronger than that of the Fe-depleted sample. The magnetization
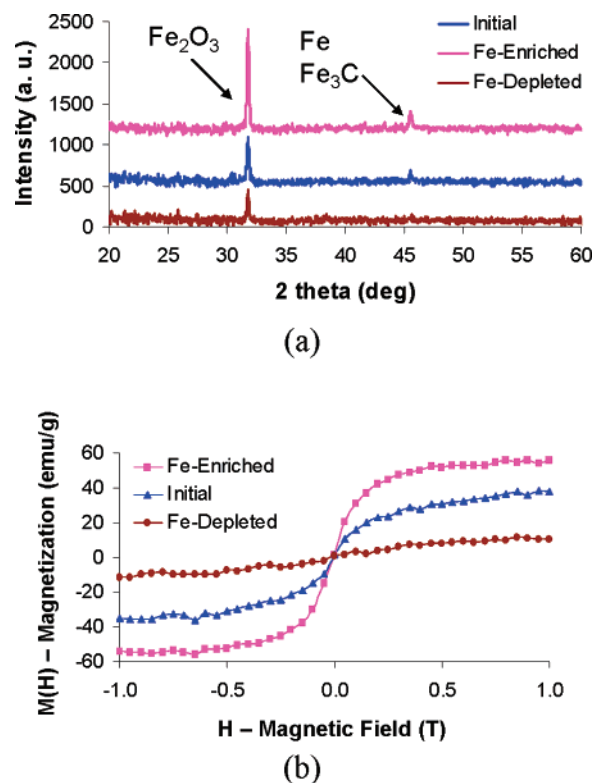

(a)

(b)

Figure 3. (a) X-ray diffraction and (b) SQUID measurements of the initial, Fe-enriched, and Fe-depleted nanotube samples. The XRD reveals that the iron particles are mainly Fe_2O_3, and the absence of hyteresis in the SQUID indicates the superparamagnetism of the Fe_2O_3 nanoparticles.

saturation values of the Fe-enriched, initial, and Fe-depleted nanotube samples are 56, 38, and 11 emu/g. Here, the magnetization values were normalized with the total mass of the nanomaterials in each sample to differentiate the magnetic responses of the samples. The results indicate that
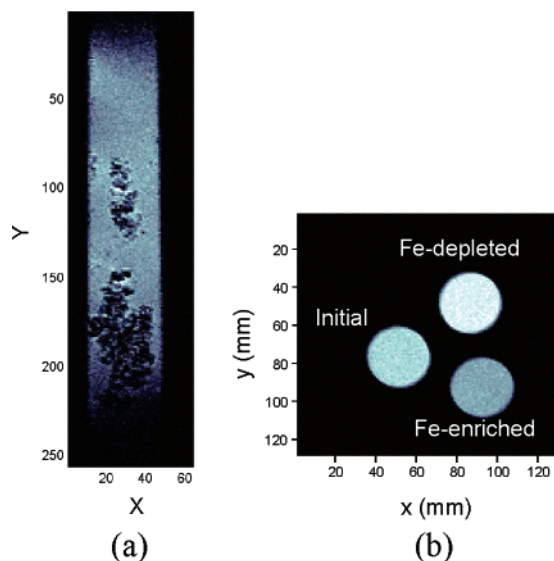
Figure 4. (a) Vertical MR image of murine macrophage cells with the Fe-enriched SWNT sample. A T_2-weighted spin−echo multislice sequence (SEMS) is used with a pulse repetition time (T_R) of 1.2 s and an echo time (T_E) of 10 ms. There are 256 pixels in the y-axis and 64 pixels in the x-axis. Each pixel has 30 μm × 30 μm in plane and 250 μm in depth. (b) Transverse MR image of the initial, Fe-enriched, and Fe-depleted nanotube samples in water (SEMS, $T_R = 1$ s and $T_E = 13$ ms). A discrete contrast is observed according to the concentration of the iron oxide nanoparticles.

the major magnetic component of the complexes is the Fe_2O_3 core rather than the nanotube itself, and the SWNT/iron oxide complexes are effectively separated from the initial stock solution while maintaining their fluorescence properties. Note that the Fe-enriched sample does not exhibit any observable magnetic remnance or hysteresis, suggesting that permanent magnetic dipoles cannot be induced within these complexes. The main reason is that the iron oxide particles are superparamagnetic and 2−5 nm in diameter, about an order of magnitude smaller than those of the iron oxide particles that are known to exhibit ferromagnetic properties.[20] The saturation magnetization of the Fe-enriched sample is in reasonable agreement with that of dextran-coated superparamagnetic iron oxide nanoparticles.[21,22]

Figure 4a shows a MR image of macrophage cells incubated with the Fe-enriched sample. The cell image is generated on a T_2-weighted spin−echo multislice sequence (SEMS) with a pulse repetition time (T_R) of 1.2 s and an echo time (T_E) of 10 ms. The image is 7.68 mm × 1.92 mm in size with 256 × 64 pixels, each of which represents 30 μm × 30 μm in plane and 250 μm in depth. Here, the macrophage cells are specifically chosen because they are involved in the immune defense systems of vertebrate animals by engulfing pathogens and can easily incorporate extraneous particles via phagocytosis. The cells were incubated with the Fe-enriched sample for a nanotube concentration of 10 mg per liter of the cell medium. After a 7 h incubation, the exact amount of the nanostructures engulfed by the cells is unknown, but the MR image clearly shows the cells as dark spots. Because the iron oxide nanoparticles are T_2 agents, the nanoparticles reduce the overall T_2 significantly, enhancing the negative image contrast. Control

experiments with cells incorporated with the Fe-depleted sample and without any nanomaterials provided no image contrast under the same measurement condition (not shown). We also imaged the cross-sections of capillary tubes containing the three nanotube samples in pure water (Figure 4b). This image is obtained based on a T_2-weighted SEMS with $T_R = 1$ s and $T_E = 13$ ms. One can readily identify the differences in the image contrast: the dark, intermediate, and light-gray areas correspond to the Fe-enriched, initial, and Fe-depleted samples, respectively.

We quantified the differences in the image contrasts created by the samples with different iron content by measuring their magnetic relaxation time scales in Intralipid. Intralipid is chosen here as a viscous matrix in which to disperse the particles, not for its scattering properties as it is usually employed. T_2 relaxation time was determined based on the Carr−Purcell−Meiboom−Gill (CPMG) sequence with $T_R = 4$ s and $T_E = 93$ ms, whereas T_1 time was obtained based on the inversion recovery sequence ($T_R = 5$ s). With the nanotube concentration of 4 mg/L in the Intralipid, the initial, Fe-enriched, and Fe-depleted samples have $T_1 = 2.52$ s and $T_2 = 261$ ms, $T_1 = 1.91$ s and $T_2 = 164$ ms, and $T_1 = 1.98$ s and $T_2 = 341$ ms, respectively. The pure Intralipid with no sample added has $T_1 = 1.67$ s and $T_2 = 498$ ms. T_2 decreases with increasing iron oxide particle concentration, and the Fe-enriched sample certainly shows the shortest T_2 among the samples. The iron oxide particles predominantly affect T_2, although T_1 and T_2 are not completely independent.[20] Better contrast can be obtained in T_2-weighted images when materials with lower T_1/T_2 ratios as well as greater relaxivities are used. The T_1/T_2 ratio of the Fe-enriched sample is approximately 12, comparable to the previously reported values of the conventional MRI iron oxide particle agents ($T_1/T_2 = 2$−15).[20−22,42] We note that the spin−spin relaxation time (T_2) measured here, however, is an order of magnitude longer than Cy5.5 dye-attached iron oxide nanoparticles[30] because the iron oxide nanoparticles of the complexes have 2−3 times smaller diameters.

We also used the SWNT component of the complexes as NIR fluorophores to image the macrophage cells. The image of the cells incorporated with the Fe-enriched sample is obtained with an optical microscope, as shown in Figure 5a, where each tick marker represents 2 μm. These cells grow and divide rapidly, forming clusters of cells as observed in the image. Figure 5a also includes an overlaid area map constructed by integrating the (8,3) and (6,5) SWNT fluorescence from 958 to 1027 nm, corresponding to 2300−3000 cm^{-1} in the Raman spectra. Two Raman spectra obtained at the locations **1** and **2** in the cell image are shown in Figure 5b. The cells are plated on a glass slide so that the glass features are seen when compared to the Raman spectra from the sample solution contained in a quartz cuvette (Figure 2c). The spectra and map were taken by irradiating 785 nm light (36 mW) for 20 s through a 50× magnification objective lens. The laser spot size was approximately 12 μm in diameter assuming a Gaussian beam. It is important to note that the incubated cells were washed prior to measurement to ensure that no free complexes were present outside
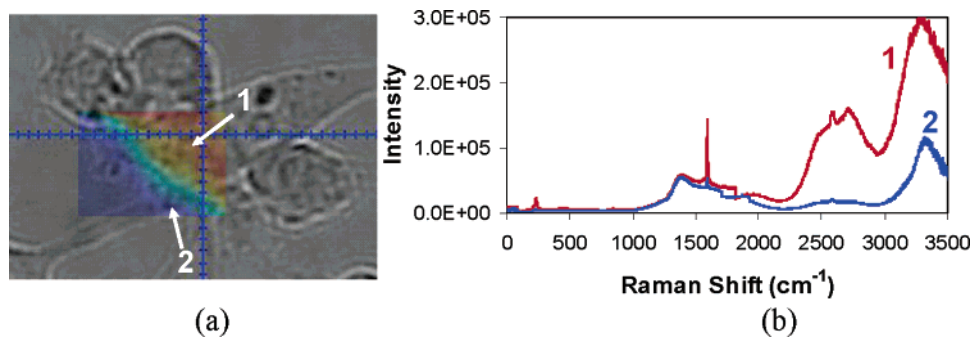
Figure 5. (a) Image of macrophage cells incorporated with the Fe-enriched SWNT sample through an optical microscope. Each tick marker represents 2 μm. An area map of NIR fluorescence (958−1027 nm, corresponding to 2300−3000 cm^{-1} in Raman spectra) from the complexes is overlaid. (b) Raman spectra obtained at two different locations, **1** and **2** in (a). A 785 nm laser diode was used for excitation at 36 mW through a 50× magnification objective lens. The NIR map shows the cell boundaries, where the bright-red areas represent the cell that contains the Fe-enriched DNA-SWNT while the dark-blue region indicates the absence of SWNT either outside the cell or in the cell areas that do not contain a large amount of SWNT.

the cells. Although we could not resolve the cell structure and the precise location of the complexes due to the large beam size, the NIR map clearly shows the cell boundaries where the bright-red areas represent the cell that contains the Fe-enriched DNA-SWNT, while the dark-blue region indicates the absence of SWNT either outside the cell or in the cell areas that do not contain a large amount of SWNT. A higher-resolution optical microscope that is capable of single carbon nanotube spectroscopy would provide information of cell structures in greater detail.

The utility of multimodal nanoparticle imaging agents should be evaluated by their functionalities such as their optical and magnetic properties and biocompatibilities. First, the nanoparticle scaffolds that utilize semiconductor quantum dots and single-walled carbon nanotubes have several advantages over conventional organic dye-based probes: their fluorescence is distinct, tunable, and photostable. Moreover, biologically transparent NIR fluorescing nanomaterials are favored for in vivo imaging and cell labeling. The complexes can be employed as photodynamic therapy agents because carbon nanotubes have exceptionally large absorption cross-sections in the near-infrared.[43] Second, magnetic nanoparticles that have strong magnetic responses are preferred so that they can not only be used for MRI but can also be manipulated by an external magnetic field. The saturation magnetization of nanoparticles made of FeCo[33] and Co[44,45] is 2−3 times greater than that of iron oxide nanoparticles. We attempted to magnetically modulate the complexes with a 0.02 T solenoid system, but the magnetic force was not sufficient to overcome Brownian motion, as the magnetic force exerted on a particle is proportional to the volume of the magnetic component.[26] Recent reports showed that CdSe quantum dots encapsulating a ∼10 nm magnetic core had a ∼70% lower emission quantum yield[46] and a ∼90% shorter lifetime[45] than the original quantum dots. In contrast, the optical properties of SWNT in this study are not significantly affected by the presence of the iron oxide nanoparticles. Lastly, the DNA encapsulation renders the complexes water-soluble, biocompatible, and most importantly, optically active in live cells for up to 3 months.[10] The present study suggests that the potential application of these complexes for in vivo imaging depends now upon molecular chemistry to functionalize the complexes to target specific proteins, tumors, and cancer cells.

Conclusions. In this study, we demonstrated for the first time the use of the SWNT/iron oxide nanoparticle complexes as multimodal biomedical imaging agents. The individually suspended complexes in water were prepared by wrapping the HiPco-produced SWNT with DNA, followed by magnetic separation. We characterized the optical and magnetic properties of the nanotube samples with different iron oxide contents and imaged macrophage cells containing these nanostructures using magnetic resonance and NIR fluorescence. The results suggest that these complexes could be used to assess tissue or probe individual cells of interest. If the Fe-enriched SWNT are suspended or further functionalized with monoclonal antibodies to target specific receptor sites (e.g., integrin receptors in the development of atherosclerosis and cancer), the complexes could be used as targeted agents to provide molecular-level contrast and biosensing. Finally, the potential exists for these complexes to achieve phototherapy and hyperthermia effects in cells and tissue through NIR laser radiation and the high-speed rotation of the nanomaterials upon application of an external magnetic field modulated at a high frequency.

References

(1) Avouris, P. *Acc. Chem. Res.* **2002**, *35*, 1026−1034.

(2) Bachilo, S. M.; Strano, M. S.; Kittrell, C.; Hauge, R. H.; Smalley, R. E.; Weisman, R. B. *Science* **2002**, *298*, 2361−2366.

(3) Barone, P. W.; Baik, S.; Heller, D. A.; Strano, M. S. *Nat. Mater.* **2005**, *4*, 86−92.

(4) Hartschuh, A.; Pedrosa, H. N.; Novotny, L.; Krauss, T. D. *Science* **2003**, *301*, 1354−1356.

(5) Kono, J.; Ostojic, G. N.; Zaric, S.; Strano, M. S.; Shaver, J.; Hauge, R. H.; Smalley, R. E. *Appl. Phys. A* **2004**, *78*, 1093−1098.

(6) O'Connell, M. J.; Bachilo, S. M.; Huffman, C. B.; Moore, V. C.; Strano, M. S.; Haroz, E. H.; Rialon, K. L.; Boul, P. J.; Noon, W. H.; Kittrell, C.; Ma, J.; Hauge, R. H.; Weisman, R. B.; Smalley, R. E. *Science* **2002**, *297*, 593−596.

(7) Strano, M. S. *J. Am. Chem. Soc.* **2003**, *125*, 16148−16153.

(8) Strano, M. S.; Doorn, S. K.; Haroz, E. H.; Kittrell, C.; Hauge, R. H.; Smalley, R. E. *Nano Lett.* **2003**, *3*, 1091−1096.

(9) Doorn, S. K.; Heller, D. A.; Barone, P. W.; Usrey, M. L.; Strano, M. S. *Appl. Phys. A* **2004**, *78*, 1147−1155.

(10) Heller, D. A.; Baik, S.; Eurell, T. E.; Strano, M. S. *Adv. Mater.* **2005**, *17*, 2793−2799.

(11) Wray, S.; Cope, M.; Delpy, D. T.; Wyatt, J. S.; Reynolds, E. O. R. *Biochim. Biophys. Acta* **1988**, *933*, 184−192.

(12) Strano, M. S.; Moore, V. C.; Miller, M. K.; Allen, M. J.; Haroz, E. H.; Kittrell, C.; Hauge, R. H.; Smalley, R. E. *J. Nanosci. Nanotechnol.* **2003**, *3*, 81−86.

(13) Moore, V. C.; Strano, M. S.; Haroz, E. H.; Hauge, R. H.; Smalley, R. E. *Nano Lett.* **2003**, *3*, 1379−1382.

(14) Chen, X.; Tam, U. C.; Czlapinski, J. L.; Lee, G. S.; Rabuka, D.; Zettl, A.; Bertozzi, C. R. *J. Am. Chem. Soc.* **2006**, *128*, 6292−6293.

(15) Karajanagi, S. S.; Yang, H.; Asuri, P.; Sellitto, E.; Dordick, J. S.; Kane, R. S. *Langmuir* **2006**, *22*, 1392−1395.

(16) Richard, C.; Balavoine, F.; Schultz, P.; Ebbesen, T. W.; Mioskowski, C. *Science* **2003**, *300*, 775−778.

(17) Zheng, M.; Jagota, A.; Semike, E. D.; Diner, B. A.; Mclean, R. S.; Lustig, S. R.; Richardson, R. E.; Tassi, N. G. *Nat. Mater.* **2003**, *2*, 338−342.

(18) Zheng, M.; Jagota, A.; Strano, M. S.; Santos, A. P.; Barone, P. W.; Chou, S. G.; Diner, B. A.; Dresselhaous, M. S.; Mclean, R. S.; Onoa, G. B.; Samsonidze, G. G.; Semke, E. D.; Usrey, M. L.; Walls, D. J. *Science* **2003**, *302*, 1545−1548.

(19) Heller, D. A.; Jeng, E. S.; Yeung, T.-K.; Martinez, B. M.; Moll, A. E.; Gastala, J. B.; Strano, M. S. *Science* **2006**, *311*, 508−511.

(20) Mornet, S.; Vasseur, S.; Grasset, F.; Duguet, E. *J. Mater. Chem.* **2004**, *14*, 2161−2175.

(21) Jung, C. W.; Jacobs, P. *Magn. Reson. Imaging* **1995**, *13*, 661−674.

(22) Bulte, J. W. M.; Brooks, R. A.; Moskowitz, B. M.; Bryant, L. H., Jr.; Frank, J. A. *Magn. Reson. Med.* **1999**, *42*, 379−384.

(23) Wada, S.; Yue, L.; Tazawa, K.; Furuta, I.; Nagae, H.; Takemori, S.; Minaminura, T. *Oral Dis.* **2001**, *7*, 192−195.

(24) Brasch, R. C. *Magn. Reson. Med.* **1991**, *22*, 282−287.

(25) Oldenburg, A. L.; Gunther, J. R.; Boppart, S. A. *Opt. Lett.* **2005**, *30*, 747−749.

(26) Oldenburg, A. L.; Toublan, F. J.; Suslick, K. S.; Wei, A.; Boppart, S. A. *Opt. Exp.* **2005**, *13*, 6597−6614.

(27) Cai, D.; Mataraza, J. M.; Qin, Z.-H.; Huang, Z.; Huang, J.; Chiles, T. C.; Carnahan, D.; Kempa, K.; Ren, Z. *Nat. Methods* **2005**, *2*, 449−454.

(28) Huh, Y.-M.; Jun, Y.-w.; Song, H.-T.; Kim, S.; Choi, J.-s.; Lee, J.-H.; Yoon, S.; Kim, K.-S.; Shin, J.-S.; Suh, J.-S.; Cheon, J. *J. Am. Chem. Soc.* **2005**, *127*, 12387−12391.

(29) Talanov, V. S.; Regino, C. A. S.; Kobayashi, H.; Bernardo, M.; Choyke, P. L.; Brechbiel, M. W. *Nano Lett.* **2006**, *6*, 1459−1463.

(30) Veiseh, O.; Sun, C.; Gunn, J.; Kohler, N.; Gabikian, P.; Lee, D.; Bhattarai, N.; Ellenbogen, R.; Sze, R.; Hallahan, A.; Olson, J.; Zhang, M. *Nano Lett.* **2005**, *5*, 1003−1008.

(31) Rieter, W. J.; Taylor, K. M. L.; An, H.; Lin, W.; Lin, W. *J. Am. Chem. Soc.* **2006**, *128*, 9024−9025.

(32) Zebli, B.; Susha, A. S.; Sukhorukov, G. B.; Rogach, A. L.; Parak, W. J. *Langmuir* **2005**, *21*, 4262−4265.

(33) Seo, W. S.; Lee, J. H.; Sun, X.; Suzuki, Y.; Mann, D.; Liu, Z.; Terashima, M.; Yang, P. C.; McConnell, M. V.; Nishimura, D. G.; Dai, H. *Nat. Mater.* **2006**, *5*, 971−976.

(34) Nikolaev, P.; Bronikowski, M. J.; Bradley, R. K.; Rohmund, F.; Colbert, D. T.; Smith, K. A.; Smalley, R. E. *Chem. Phys. Lett.* **1999**, *313*, 91−97.

(35) Bronikowski, M. J.; Willis, P. A.; Colbert, D. T.; Smith, K. A.; Smalley, R. E. *J. Vac. Sci. Technol.* **2001**, *19*, 1800−1805.

(36) Hafner, J. H.; Bronikowski, M. J.; Azamian, B. R.; Nikolaev, P.; Rinzler, A. G.; Colbert, D. T.; Smith, K. A.; Smalley, R. E. *Chem. Phys. Lett.* **1998**, *296*, 195−202.

(37) Dai, H.; Rinzler, A. G.; Nikolaev, P.; Thess, A.; Colbert, D. T.; Smalley, R. E. *Chem. Phys. Lett.* **1996**, *260*, 471−475.

(38) Heller, D. A.; Mayrhofer, R. M.; Baik, S.; Grinkova, Y. V.; Usrey, M. L.; Strano, M. S. *J. Am. Chem. Soc.* **2004**, *126*, 14567−14573.

(39) Heller, D. A.; Barone, P. W.; Swanson, J. P.; Mayrhofer, R. M.; Strano, M. S. *J. Phys. Chem. B* **2004**, *108*, 6905−6909.

(40) Schnitzler, M. C.; Oliveira, M. M.; Ugarte, D.; Zarbin, A. J. G. *Chem. Phys. Lett.* **2003**, *381*, 541−548.

(41) Usrey, M. L.; Lippmann, E. S.; Strano, M. S. *J. Am. Chem. Soc.* **2005**, *127*, 16129−16135.

(42) Bulte, J. W. M.; Cuyper, M. D.; Frank, J. A. *J. Magn. Magn. Mater.* **1999**, *194*, 204−209.

(43) Kam, N. W. S.; O'Connell, M. J.; Wisdom, J. A.; Dai, H. *Proc. Natl. Acad. Sci. U.S.A.* **2005**, *102*, 11600−11605.

(44) Dumestre, F.; Chaudret, B.; Amiens, C.; Fromen, M.-C.; Casanove, M.-J.; Renaud, P.; Zurcher, P. *Angew. Chem., Int. Ed.* **2002**, *41*, 4286−4289.

(45) Kim, H.; Achermann, M.; Balet, L. P.; Hollingsworth, J. A.; Klimov, V. I. *J. Am. Chem. Soc.* **2005**, *127*, 544−546.

(46) Wang, D.; He, J.; Rosenzweig, N.; Rosenzweig, Z. *Nano Lett.* **2004**, *4*, 409−413.